A New Era in Ceramic Archaeometry: A Comprehensive Multimodal Methodological Workflow

R. Abdelrahman[a,b], J. Depciuch[c], P. Grzywa[a], S. Wroński[a], L. Alluhaibi[d], M. Środa[e], A. Maximenko[d], M. Wojenka[f], J. Tarasiuk[a] and L. Samek[a,*]

[a] *AGH University of Kraków, Faculty of Physics and Applied Computer Science, al. Mickiewicza 30, 30-059 Kraków, Poland*
[b] *Future University in Egypt, Faculty of Engineering and Technology, 90th Street, Fifth Settlement, New Cairo, 11835 Cairo, Egypt*
[c] *Institute of Nuclear Physics Polish Academy of Science, Radzikowskiego 152, 31-342 Kraków, Poland*
[d] *SOLARIS National Synchrotron Radiation Centre, Jagiellonian University, Czerwone Maki 98, 30-392 Kraków, Poland*
[e] *AGH University of Kraków, Faculty of Materials Science and Ceramics, al. Mickiewicza 30, 30-059 Kraków, Poland*
[f] *Jagiellonian University Institute of Archaeology, Gołębia 11, 31-007 Kraków, Poland*

Received: 30.12.2025 & Accepted: 17.04.2026

Doi: 10.12693/APhysPolA.149.S198 *e-mail: Lucyna.Samek@fis.agh.edu.pl

This study establishes a comprehensive, sequential multimodal workflow for archaeometric analysis of medieval ceramics, integrating seven measurement techniques to characterize elemental, crystalline, amorphous, microstructural, structural, and chemical-state properties of the material, while preserving artefact integrity. Therefore, (i) X-ray fluorescence establishes baseline major (Si, Al, Fe, Ca, K, Na) and trace (Cr, Mn, Zr) profiles for paste discrimination; (ii) X-ray diffraction identifies kaliophilite/oligoclase phases ($\sim$ 800–900°C firing); (iii) Fourier transform infrared resolves amorphous networks (Si–O–Si 950–1100 cm^{-1}); (iv) Raman spectroscopy detects microscale oxide impurities (anatase TiO_2 lattice modes at 110–160 cm^{-1}, ZrO_2, Al_2O_3 corundum M–O stretching modes at 440–465 cm^{-1}) and lattice defects, revealing heavy mineral tempers (rutile sands) and refractory phases undetectable by bulk diffraction analysis or the broad spectral envelopes of infrared spectroscopy; (v) scanning electron microscope with energy dispersive spectroscopy quantifies temper distributions; (vi) X-ray computed tomography reveals 3D void networks, and (vii) X-ray absorption near-edge structure constrains speciation of Fe^{2+}/Fe^{3+}, Ca carbonate–silicates, and K-feldspars. This standardized framework enables precise reconstruction of provenance, fluxing strategies, pyrotechnology, and post-firing alterations, beyond the limitations of single- and dual-technique approaches, providing a reproducible protocol for heritage science.

topics: medieval ceramics, multimodal analytical framework, archaeometry, cultural heritage

1. Introduction

Archaeological ceramic research has since been a pillar of study of material culture heritage, providing valuable perspectives on technological practices, resource-acquisition networks, craft traditions, and historical socioeconomic networks. Medieval ceramic assemblages carry complex signatures of production practices, local geology, and firing technologies [1]. However, despite their value, ceramic materials are extremely difficult to analyse due to their heterogeneous structure, multi-phase mineralogy occurring after the firing process, and the variety of thermal and post-depositional changes they undergo. These characteristics challenge researchers seeking to reconstruct manufacturing processes or determine provenance. Traditional approaches based on a single technique, whether chemical, structural, or mineralogical, provide only partial information. A single approach is prone to incomplete or ambiguous interpretations, since no single analytical approach can fully resolve the elemental, microstructural, molecular, and crystalline properties of archaeological ceramics. As analytical questions in archaeometry have grown more sophisticated, there is an increasing need for integrative, multi-scale methodologies.

Historical ceramics have been studied with a wide variety of analytical instruments, such as Fourier transform infrared (FTIR) spectroscopy [2], portable X-ray fluorescence (XRF) and Raman spectroscopy [3, 4], μ-Raman spectroscopy [5], synchrotron-based X-ray methods [6] and X-ray micro-computed tomography (XCT) [7]. The literature increasingly emphasises the need for methodological reproducibility and powerful calibration protocols in heritage science. A recent study combining XRF and XCT has shown the value of integrating elemental composition and internal structural data within a unified workflow [8]. Even the most sophisticated two-technique methods, such as the latest XRF–XCT analysis of medieval ceramics from the Kraków Upland, are still insufficient, as they neither provide molecular or crystalline information nor answer questions about firing conditions, mineral transformations, or chemical speciation. In other words, the field of ceramic characterization does not have a standardized, comprehensive, and reproducible multimodal approach that is able to address the entirety of the complexity of ceramic material. To address persistent gaps in single-technique limitations, this study employs an analytical strategy that uses a sequential multi-model workflow to characterize the elemental, mineralogical, and microstructural properties of archaeological ceramics for provenance and firing reconstruction. Initial X-ray fluorescence (XRF) analysis established bulk elemental compositions and trace-element profiles, providing a chemical baseline for each sample [9]. This was followed by X-ray diffraction (XRD) to quantify crystalline phases such as kaliophilite ($KAlSiO_4$), oligoclase, and tectosilicates, whose stability fields were constrained by peak firing temperatures ($\sim$ 800–900°C) and alkali-rich paste transformations. However, higher firing temperatures induced extensive feldspar vitrification, forming amorphous glassy matrices that obscured low-abundance and poorly crystalline phases beyond the XRD detection limits [10]. To resolve this, FTIR spectroscopy targeted the amorphous aluminosilicate networks via the Si–O–Si (950–1100 cm^{-1}) and Al–O–Si (500–800 cm^{-1}) vibrational modes, elucidating dehydroxylation states and thermal maturity that are inaccessible to diffraction [11]. Raman spectroscopy provides unique detection of microscale oxide impurities and lattice defects in these archaeological ceramics, revealing temper additives or contamination sources that are undetectable by XRD's bulk crystallinity bias or FTIR's broad vibrational envelopes. Low-frequency bands (110–160 cm^{-1}) signal lattice modes of TiO_2 (anatase) or ZrO_2, indicating accessory heavy mineral tempers (e.g., rutile sands) in feldspar-rich pastes, while 440–465 cm^{-1} M–O stretches pinpoint Al_2O_3 (corundum A_{1g} vibration) or CeO_2, suggesting refractory phases from high-alumina clays or post-firing impurities absent in XRD due to low abundance [12]. Building on these spectroscopic insights, techniques such as scanning electron microscope with energy dispersive spectroscopy (SEM–EDS) have enabled the resolution of micro- to nanoscale textural features (grain boundaries, pores, reaction rims), revealing clay fabric and sintering [13]. In turn, XCT provided non-destructive 3D volumetric mapping, quantifying the distribution of inclusions and voids, showing variations in clay refinement degree, and indicating manufacturing techniques [8]. Synchrotron X-ray absorption near-edge structure (XANES) analysis at the K-edges of Fe, Ca, and K will uniquely quantify Fe^{2+}/Fe^{3+} redox ratios, Ca carbonate–gehlenite transitions, and K feldspar-kaliophilite speciation, revealing kiln atmospheres, fluxing efficiency, and reaction interfaces unattainable by laboratory methods. This culminates in our hierarchical workflow for comprehensive pyrotechnological reconstruction [14].

This study develops a comprehensive, reproducible multi-proxy workflow that integrates XRF, XRD, FTIR, Raman, SEM–EDS, XCT, and synchrotron XANES to fully characterize the elemental, mineralogical, microstructural, and redox properties of medieval ceramics. This enables a precise reconstruction of provenance, firing technologies, manufacturing practices, and post-firing alterations, thereby surpassing the limitations of single or dual-technique approaches.

2. Materials and methods

2.1. Analytical framework of the multimodal approach

Building on the challenges outlined in Sect. 1, this section outlines the conceptual basis of the multimodal analytical framework applied in this study (see Fig. 1). The framework was designed to combine complementary methods that deliver chemical, structural, molecular, and redox information while preserving the integrity of medieval ceramic artefacts through a predominantly non-destructive and minimally destructive strategy.

Given the intrinsic heterogeneity of medieval pottery, which comprises complex firing-induced mineral transformations, mixed crystalline-amorphous matrices, varied elemental and molecular compositions, and post-depositional alterations, no single technique can adequately resolve its technological, mineralogical, and chemical complexity. A multi-scale analytical package is therefore required, capable of spanning bulk elemental composition, internal 3D structure, crystalline phase assemblages, molecular bonding environments, and local chemical speciation.

Accordingly, the workflow follows a deliberately tiered sequence (Fig. 1). At the first level, bulk chemical and phase characterization is obtained

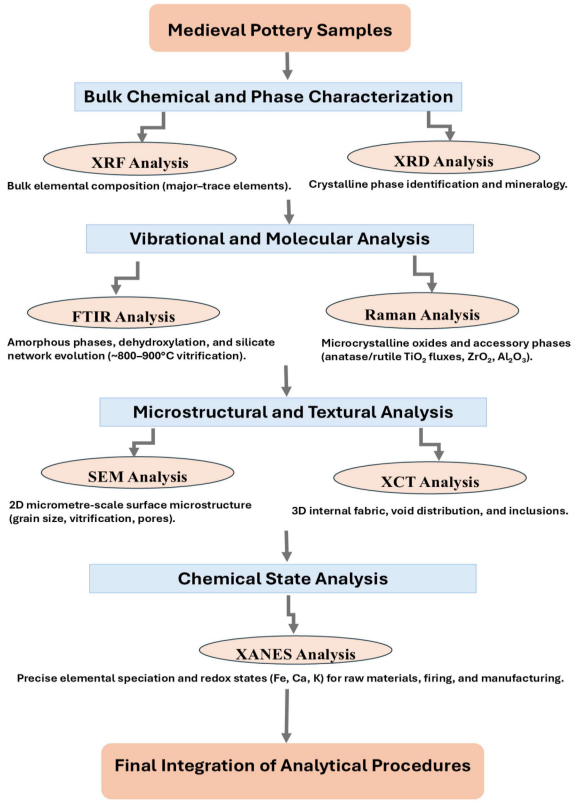

Fig. 1. Flow chart outlining the sequential structure and integration of analytical techniques applied within the multimodal framework.

using non-destructive X-ray fluorescence (XRF) and X-ray diffraction (XRD). XRF determines the abundances of major and trace elements, while XRD identifies the crystalline mineralogy. At the second level, vibrational and molecular information is acquired by Fourier transform infrared (FTIR) and Raman spectroscopy, which probe amorphous phases, silicate network evolution, dehydroxylation, and oxide/silicate micro-environments. At the third level, microstructural and textural features are resolved using scanning electron microscopy with energy-dispersive spectroscopy (SEM–EDS) and X-ray computed tomography (XCT), which characterize surface microstructures, grain boundaries, pores, and reaction rims. At the same time, XCT non-destructively quantifies the 3D distribution of internal fabric in the form of voids and inclusions.

Finally, chemical state analysis is achieved by synchrotron X-ray absorption near-edge structure (XANES), which constrains Fe, Ca, and K speciation and redox states in both crystalline and amorphous domains. Together, these linked tiers form an integrated multimodal framework that maximizes information recovery on provenance, firing technology, and post-firing alteration while maintaining the conservation requirements of cultural heritage materials.

2.2. Sample preparation

Building on the conceptual framework outlined above, this section describes how the multimodal analytical workflow is implemented in practice. It details sample preparation, instrument settings, and analysis guidelines for each technique in the sequence shown in Fig. 1 and summarised in Table I. The workflow follows a tiered order, combining non-destructive (XRF, XCT) and minimally destructive (XRD, FTIR, Raman, SEM–EDS, XANES) methods to obtain elemental, structural, molecular, mineralogical, microstructural, and redox information while preserving artefact integrity.

Table I reports the sample form, degree of (non-)destructiveness, and main preparation requirements for each method. For minimally destructive bulk and spectroscopic techniques (XRD, FTIR, Raman, SEM–EDS, and XANES), small, powdered samples were taken from both the surface (including slips or glazes where present) and interior zones.

2.3. X-ray fluorescence (XRF) analysis

X-ray fluorescence (XRF) was selected as the first analytical step in the multimodal workflow because it provides rapid, non-destructive elemental characterization of whole ceramic sherds. XRF establishes baseline major (e.g., Si, Al, Fe, Ca, K, Na) and trace (e.g., Cr, Zr, Mn, Zn) profiles, serving as an initial technique for characterizing the overall ceramic composition before guiding subsequent analyses. This baseline compositional information guides subsequent analytical stages and supports comparisons across samples. The overall XRF analytical workflow, including sample positioning and instrument setup, is illustrated in Fig. 2. Ceramic samples from the study were investigated using the advanced XRF technique at the Faculty of Physics and Applied Computer Science of the AGH University of Krakow. Analysis was conducted using a BRUKER M4 Tornado Plus spectrometer, enabling non-invasive, non-destructive sample examination. The X-ray fluorescence method requires no preliminary sample preparation; the amounts of energy deposited in the analysed material are minor and cause no changes or damage, which is very important for studing historic samples. XRF operates by directing primary X-rays onto the sample's surface, causing the atoms to undergo inner-shell ionization. When electrons from higher energy levels fill these vacancies, the atoms emit secondary (fluorescent) X-rays with energies unique to each element. By detecting and measuring these characteristic emissions, the technique enables precise identification and quantification of the elements present

TABLE I

Comparative overview of sample form, destructiveness, and preparation requirements for each analytical technique applied in this study.

Technique	Sample form	Type	Main preparation steps
XRF	whole sample	non-destructive	– Gently clean the surface to remove dust and contaminants. – Select several clean measurement points on uneven surfaces. – Ensure stable placement in the vacuum chamber.
XRD	powdered fragments or flat surfaces of small exhibits	minimally destructive	– Use fine micro-sampling to obtain a homogeneous powder grind to reduce crystallite orientation effects. – Load a thin, evenly distributed layer onto the sample holder to sensure stable Cu K_α beam conditions and appropriate scan geometry for reliable phase identification.
FTIR	powdered fragments	minimally destructive	– Perform controlled micro-sampling to obtain powdered material. – Place the sample directly onto the attenuated total reflectance (ATR) diamond crystal for analysis. – Clean the crystal thoroughly with ethanol between consecutive samples to prevent cross-contamination. – Apply baseline correction and vector normalisation to all acquired spectra before data interpretation.
Raman	powdered fragments	minimally destructive	– Perform controlled micro-sampling to obtain powdered material. – Place powdered material onto a CaF_2 window to avoid spectral interference. – Optimise laser wavelength and power to minimise fluorescence and thermal alteration.
SEM–EDS	small fragment	minimally destructive	– Cut a small fragment from the sherd. Optionally, embed it in epoxy to prepare a polished cross-section. – Grind and polish the surface to expose grains, pores, and reaction rims, then coat with a thin conductive layer (carbon or Au/Pd) before imaging and EDS analysis.
XCT	whole sample	non-destructive	– Gently clean externally to avoid loose particles. – Secure mounting of intact sherd to prevent movement. – Optimise scan geometry and apply appropriate filtering (like Cu filter) to reduce beam hardening.
XANES	powdered fragments	minimally destructive	– Perform controlled micro-sampling to obtain powdered material for both outer and inner surface. – Seal powders with Kapton tape before mounting. – Prepare reference compounds in the same manner to maintain consistency.

without altering the material's physical integrity. This method allows for qualitative analysis (identifying the elements in the sample) and quantitative analysis (determining the content of elements). Knowledge of elemental composition is helpful in determining the origin of raw materials, technological processes related to the place of production, or the chronology of the creation of artifacts being studied. Due to the requirement to conduct measurements in a completely non-destructive manner and the highly varied, heterogeneous topology of the samples (absence of flat surface areas), measurements were performed at points on the sample surface, and the obtained results were averaged. Averaging multiple points was essential to reduce the influence of mineral inclusions, surface irregularities, and firing-related heterogeneity commonly observed in medieval ceramics. Measurements were carried out in a vacuum chamber with air pressure reduced to 2 mbar. An X-ray tube with a rhodium anode, operating at an accelerating voltage of 50 kV and a maximum current of 600 μA, was used to excite characteristic elemental radiation. The samples were illuminated directly, without preliminary filtration, by a primary beam of X-ray radiation focused using a polycapillary lens to a diameter of about 20μm. Point measurements were made by illuminating with a radiation beam. The characteristic radiation excited in the sample was registered by two silicon drift detectors (SDDs) with an

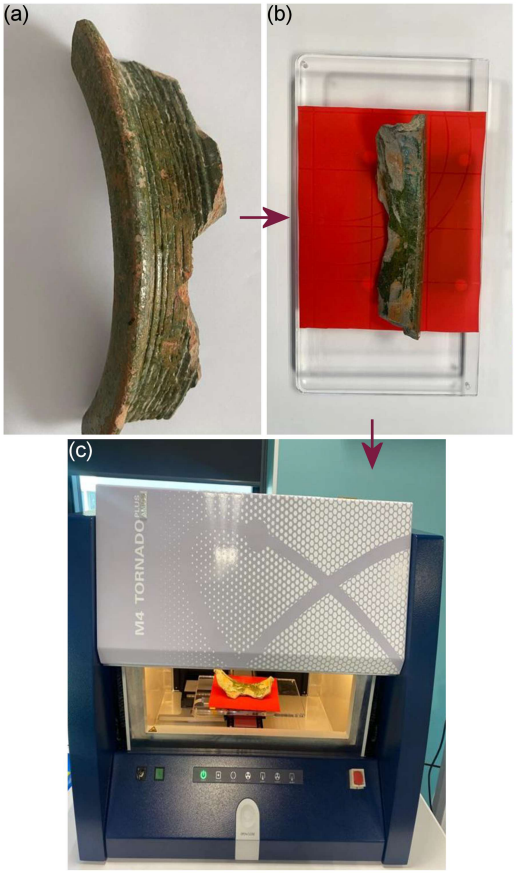

Fig. 2. Sample preparation and XRF analysis workflow. (a) A 16th-century pottery sherd prior to analysis, (b) sample positioned on the measurement stage for surface point acquisition, and (c) BRUKER M4 Tornado Plus XRF spectrometer used for non-destructive elemental analysis.

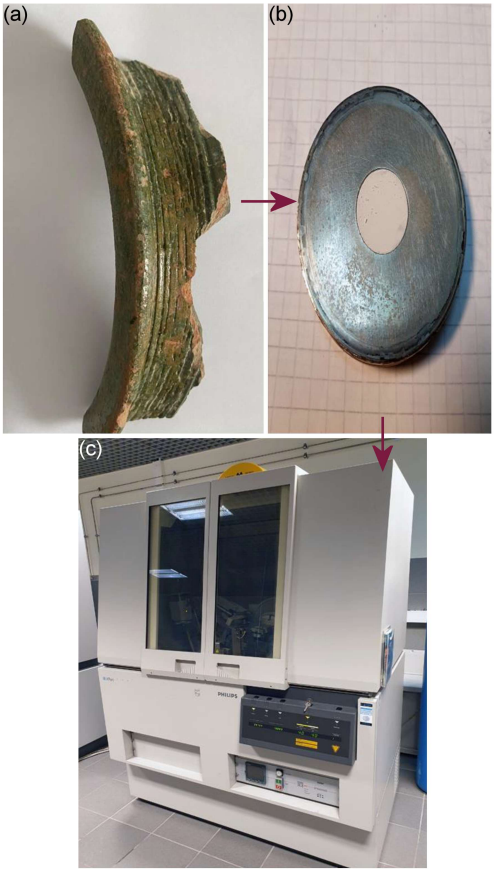

Fig. 3. Sample preparation and XRD analysis workflow. (a) A 16th century pottery fragment, (b) powdered sample mounted in an aluminium sample holder for XRD measurement, and (c) X-ray diffractometer setup used for analysis.

energy resolution capability of (full width at half maximum) FWHM = 150 eV at 5.9 keV, a thickness of 0.45 mm, equipped with ultra-thin windows with an area of 60 mm^2.

2.4. X-ray diffraction (XRD) analysis

The second analytical procedure in the multimodal workflow is X-ray diffraction (XRD), which determines crystalline phases in powdered ceramic material to interpret firing conditions, mineral transformations (e.g., kaliophilite from K fluxes, oligoclase from Na and Ca), and technological decisions. XRD adds critical phase identification that confirms the presence of neoformed minerals predicted by prior XRF elemental profiles (high K and Ca), linking bulk chemistry to firing technology and paste group discrimination, although it does not detect amorphous glassy matrices resulting from feldspar vitrification. Figure 3 is a representation of the overall XRD analytical workflow — the preparation of the powdered sample and the diffractometer setup. Small ceramic samples were micro-sampled and gently ground into a fine, homogeneous powder, taking care not to disorient the crystallites. This is the aim of powder diffraction analysis. The fine material was spread on the sample holder in a fine layer to ensure that no favoured orientation effect is produced. XRD is a technique that involves the incidence of monochromatic X-rays on a powdered sample and the capture of diffraction pattern caused by constructive interference of X-rays scattered by reflection from ordered planes of atoms in crystalline substances. In the case where the Bragg law ($2d\sin(\theta) = n\lambda$) is satisfied, diffraction peaks appear at specific angles corresponding to the interplanar spacings (d values). This enables the identification of crystalline phases based on their unique diffraction patterns. Measurements of all XRDs were made by a PANalytical X'Pert Pro diffractometer, which is a two-circle goniometer system with a goniometer radius of 240 mm. The instrument can be used in both Bragg–Brentano and parallel-beam geometries. The X-ray source was a copper-anode tube

(Cu K_{α_1} radiation), monochromatized using a Johansson or flat mirror, depending on the selected geometry. The system has two replaceable detectors, i.e., a semiconductor strip detector and a proportional counter, enabling a flexible measurement setup. Small volumes of material, a few grams, can be placed in the sample holder, and depending on the sample, low-angle grazing-incidence diffraction (GID) and high-temperature measurements up to 1400°C can be performed where needed. In every single measurement, the tube voltage and current were adjusted to stabilise the intensity of the primary X-ray beam to enable effective comparison of peak intensities. Phase identification was carried out by analysing the diffraction patterns, estimating the interplanar spacings and relative intensities of individual diffraction peaks, and comparing them with reference data available in the ICDD PDF4+ crystallographic database (ICDD — International Centre for Diffraction Data; PDF — powder diffraction patterns). This enabled qualitative identification of the constituent mineral phases and, where applicable, semi-quantitative determination of their relative peak intensities. XRD measurements were performed at the AGH University of Krakow, Faculty of Materials Science and Ceramics, Kraków, Poland.

2.5. Fourier transform infrared spectroscopy (FTIR) analysis

The third analytical procedure is Fourier transform infrared (FTIR) spectroscopy, which characterizes amorphous aluminosilicate networks via Si–O–Si (950–1100 cm^{-1}) and Al–O–Si (500–800 cm^{-1}) vibrational modes in powdered ceramic matrix. FTIR complements XRD limitations by revealing dehydroxylation states, thermal maturity, and glassy phase evolution, while validating crystalline phases through complementary absorption bands. The overall FTIR analytical workflow, including powdered sample preparation and attenuated total reflectance (ATR) instrument setup, is illustrated in Fig. 4. Small fragments were micro-sampled from non-diagnostic areas of the sherd and gently ground in an agate mortar to produce a fine, homogeneous powder suitable for infrared analysis. The powdered material was placed directly onto the ATR diamond crystal to ensure optimal contact between the sample and the internal reflection element. FTIR spectroscopy operates by passing infrared radiation through or across the sample surface and measuring the absorption of specific wavelengths associated with molecular vibrations. These absorption bands allow the identification of functional groups, clay minerals, carbonates, and firing-induced transformations within the ceramic matrix. All FTIR measurements were performed using a Nicolet IS50 FTIR spectrometer equipped with a deuterated

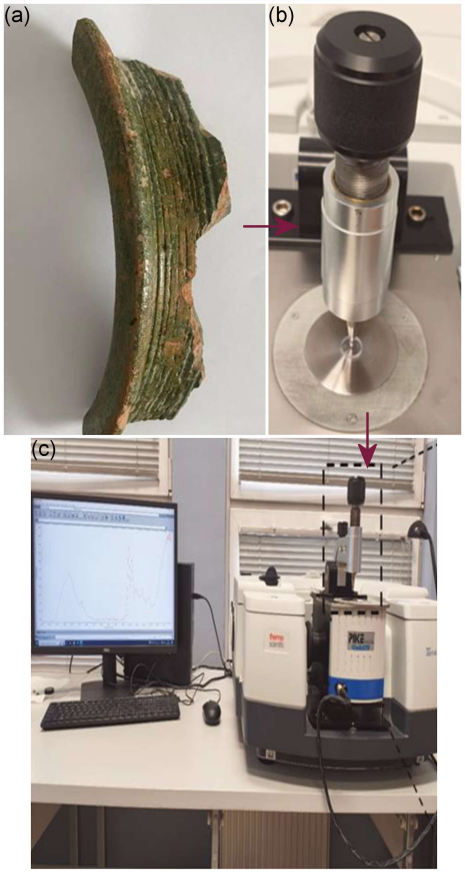

Fig. 4. Sample preparation and FTIR analysis workflow. (a) A 16th-century pottery fragment, (b) fine powdered sample placed on an ATR diamond crystal, and (c) FTIR spectrometer-microscope setup used for measurements.

triglycine sulfate (DTGS) detector. In this study, the ATR method was used. Before measurement, samples were placed on the ATR diamond crystal. After each sample, the ATR diamond crystal was cleaned using 70% ethanol. All spectra were collected from 4000 to 400 cm^{-1} at a spectral resolution of 4 cm^{-1} with 32 scans. Recordings were performed by OMNIC (Thermo Fisher Scientific, Waltham, USA) software. Baseline correction and vector normalization were done using OPUS 7.0 software. FTIR measurements were performed at the Institute of Nuclear Physics, Polish Academy of Science, Kraków, Poland.

2.6. Raman spectroscopy analysis

The fourth analytical procedure in the multimodal workflow is Raman spectroscopy, which identifies mineralogical and molecular phases in the medieval ceramic matrix and glaze via vibrational fingerprints, detecting TiO_2 and ZrO_2 inclusions and flux-driven transformations. Raman

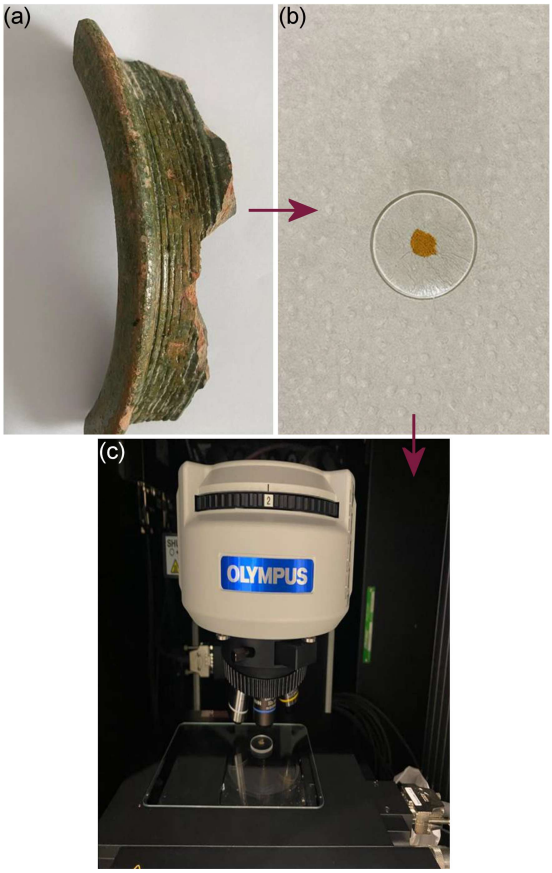

Fig. 5. Sample preparation and Raman analysis workflow. (a) A 16th-century pottery fragment, (b) fine powdered sample placed on a non-reactive CaF_2 optical window, and (c) Raman microscope setup used for vibrational spectroscopic measurement.

adds microscale phase mapping that overcomes FTIR's bulk limitations, confirming XRD/FTIR phases (kaliophilite, oligoclase) at specific sites while revealing low-abundance heavy minerals such as Zr that are linked to XRF trace profiles for enhanced provenance discrimination. The overall Raman analytical workflow, including powdered sample preparation and measurement configuration, is illustrated in Fig. 5. Small fragments were powdered and sampled from non-decorated areas of the sherd to avoid visual or structural alteration. They were gently ground in an agate mortar to produce a fine, homogeneous powder. The resulting powder was placed on a calcium fluoride (CaF_2) optical window (25 mm in dimension and 2 mm in thickness), selected for its chemical inertness and low Raman background, to ensure clean spectral acquisition. Raman spectroscopy operates by illuminating the sample with a monochromatic laser and detecting the inelastically scattered light, which undergoes energy shifts corresponding to specific molecular vibrations. These Raman shifts provide diagnostic information on mineral phases, firing-related transformations, and glaze composition. Raman measurements were conducted using a MonoVista CRS^3 500 confocal Raman microscope equipped with a laser with an excitation wavelength of 532 nm, operating at a power of 1.5–5 mW, and regulated by a (1.25–1.9) neutral-density filter. The spectrometer was fitted with 300 and 1200 lines/mm gratings, while an Olympus BX53 microscope equipped with a 50× long-working-distance objective was used for laser focusing. Spectra were recorded in the 100–4650 cm^{-1} range with an exposure time of 0.5 s and 20 accumulations per point to enhance the signal-to-noise ratio while preventing thermal alteration of the material. Data acquisition and preliminary processing, including baseline correction and normalization, were performed using Vista Control V4.9.2 (S&I GmbH). All Raman analyses were carried out at the Complementary Techniques Section of the ASTRA beamline, SOLARIS National Synchrotron Radiation Centre Jagiellonian University (Kraków, Poland).

2.7. Scanning electron microscopy with energy-dispersive X-ray spectroscopy (SEM–EDS)

The fifth analytical procedure in the multimodal workflow is scanning electron microscopy with energy-dispersive X-ray spectroscopy (SEM–EDS), which provides high 2D-resolution microstructural and microchemical characterization of medieval pottery fragments. SEM–EDS adds quantitative mineralogical mapping of the clay matrix fabrics, non-plastic inclusions (such as quartz, feldspars, Ti and Zr oxides), reaction rims, and porosity distributions. In this way, it resolves the prior bulk limitations of vibrational (Raman and FTIR) techniques by distinguishing primary tempers from firing-induced neoformed phases, allowing for raw material sourcing and pyrotechnology reconstruction. The complete SEM–EDS workflow follows automated SEM mineralogy protocols for archaeological ceramics. Analyses commenced with small fragments ($\sim 5 \times 5 \times 3$ mm) cut from representative interiors of medieval pottery sherds and fracture edges, avoiding decorated surfaces to preserve artefact integrity. The fragments were mounted in low-viscosity epoxy resin (30 mm diameter circular mounts), sequentially ground (SiC 800–4000 grit), polished to 0.25 μm diamond suspension, and coated with a 10–15 nm carbon layer to expose fresh cross-sections, preserving grain-pore-reaction rim relationships. Field-emission SEM imaging (15–20 kV, 8 mm WD) employed backscattered electrons (BSE) for phase contrast and automated EDS mapping (1024×768 pixels, 100–200 s dwell) over fields of 1500–2500 μm to quantify Si–Al–Fe–Ca–K–Ti–Zr distributions. Mineral classification via a species database yielded false-colour modal maps that report area percentage

mineralogy, grain-size distributions, and porosity networks from $n = 10$–15 fields per sherd, revealing temper selection, clay refinement quality, and sintering microstructures characteristic of medieval pyrotechnology [13].

2.8. X-ray computed tomography (XCT) analysis

The sixth analytical procedure in the multimodal workflow is X-ray computed tomography (XCT), which provides non-destructive 3D visualization of internal ceramic microstructures, including inclusions, voids, and temper distribution. XCT adds volumetric structural quantification that integrates prior microchemical (SEM–EDS) and vibrational (Raman/FTIR/XRD) data, revealing manufacturing techniques, raw material preparation, and firing inhomogeneities that are invisible to surface-limited analyses, thereby enabling comprehensive pyrotechnology reconstruction. The overall XCT analytical workflow, including sample stabilization and scanning configuration, is illustrated in Fig. 6. All XCT scans of pottery sherds were performed at the Faculty of Physics and Applied Computer Science of the AGH University of Krakow using a "nano tom 180N" device produced by GE Sensing & Inspection Technologies Phoenix X-ray Gmbh [15]. The instrument is equipped with a nanofocus X-ray tube capable of operating at voltages up to 180 kV, enabling high-resolution imaging of fine ceramic microstructural features. XCT operates by rotating the ceramic sample to transmit X-rays, simultaneosly recording variations in beam attenuation caused by differences in density and composition. As the sample rotates through 360°, a series of radiographic projections are collected. These projections are then mathematically reconstructed using a cone-beam algorithm to generate a volumetric dataset composed of virtual slices. The resulting 3D model allows visualization and quantification of the internal structure without the need for physical sectioning of the artefact. The tomograms were collected using a Hamamatsu C7942SK-25 detector (grey scale resolution of 12-bit, 2300×2300 pixels, pixel size of 50 μm). All examined samples were scanned at 60 kV of source voltage and 230 μA, with a rotation of the specimen of 360° in 1400 steps. A 0.3 mm copper filter was placed between the source and the sample to reduce beam hardening artefacts. The exposure time was 500 ms, and four frames were used for averaging to minimize detector noise. The total measurement time for each sample was ≈ 60 min. The reconstruction of measured objects was done using proprietary GE software datosX ver. 2.1.0 with the use of the Feldkamp algorithm for cone beam X-ray computed tomography (CT) [16]. The post-reconstruction data treatment was performed using VGStudio Max 2.1 [17] and Fiji (ImageJ) software. Bright regions in the reconstructed volumes correspond to components with higher X-ray absorption, such as dense mineral inclusions or compact ceramic-matrix regions. In contrast, darker regions indicate lower-density features, including voids or less compact regions in the ceramic body.

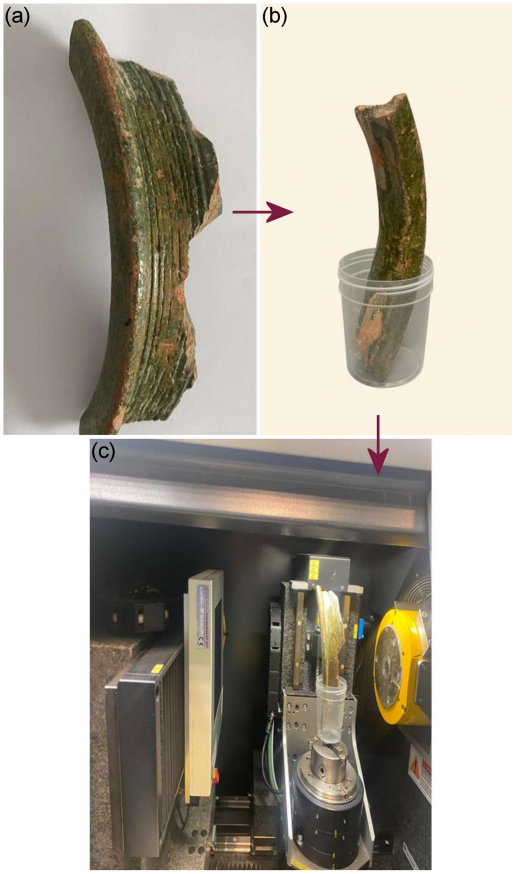

Fig. 6. Sample preparation and XCT analysis workflow. (a) A 16th century pottery fragment, (b) sample stabilized in a cylindrical holder to ensure secure and vibration-free mounting, and (c) nano CT scanning chamber of the GE Phoenix "nanotom 180N" system used for non-destructive three-dimensional imaging of internal ceramic microstructures.

2.9. X-ray absorption near-edge structure (XANES) analysis

The seventh analytical procedure in the multimodal workflow is X-ray absorption near-edge structure (XANES) spectroscopy, which determines oxidation states and local coordination environments of key elements (K, Fe, Ca) within the ceramic matrix. XANES adds chemical-state speciation that resolves prior structural (XCT/SEM–EDS) and vibrational (Raman/FTIR/XRD) limitations, quantifying Fe^{2+}/Fe^{3+}

ratios, Ca carbonate silicate transitions, and K coordination in neoformed phases (kaliophilite) to elucidate redox conditions and flux reactions during firing. The overall XANES analytical workflow, including powdered sample preparation, sample mounting, and beamline measurement configuration, is illustrated in Fig. 7. Small fragments were gently micro-sampled from non-diagnostic areas of the ceramic sherds into a fine powder, ensuring homogeneous material suitable for synchrotron-based X-ray absorption measurements. The powdered samples were sealed between layers of Kapton tape to secure them within the holders and to prevent material loss during beam exposure. XANES operates by measuring X-ray absorption as the incident photon energy is scanned across the absorption edge of the selected element. Changes in absorption intensity near the edge provide information on the oxidation state, coordination geometry, and local bonding environment, allowing detailed chemical-state characterization of the Fe-, Ca-, and K-bearing phases within the ceramic. XANES measurements were conducted at the ASTRA beamline of the SOLARIS National Synchrotron Radiation Centre, Jagiellonian University in Krakow, Poland [18, 19]. We measured XANES spectra at the K, Fe, and Ca K-absorption edges using a photon beam from a double-bend achromatic 1.3 T bending magnet ($E_c \approx 2$ keV). For these measurements, a Ge(220) crystal pair was used to monochromatize the beams. The beam size at the sample position was 7×1 mm, defined by slits. Spectra were obtained in fluorescence mode at room temperature.

For Fe K-edge measurements, the ionization chambers and the sample chamber were filled with N_2 gas at atmospheric pressure, whereas Ca and K K-edge measurements, the pressures were 100 and 80 torr, respectively. Fe foil from Exafs Company (Danville, USA) was used to calibrate the beamline at the Fe K-edges. Calibration of the K and Ca K-edge energy scales was performed using KCl and $Ca(OH)_2$ reference compounds, respectively. The K K-edge was aligned by setting the maximum of the first white-line component to 3611.0 eV, consistent with the value reported by Cibin et al. [20]. The Ca K-edge was calibrated by assigning the white-line maximum of $Ca(OH)_2$ to 4051.7 eV, in agreement with literature data [21]. Reference compounds expected in archaeological ceramics: Fe K-edge (hematite Fe_2O_3, magnetite Fe_3O_4, illite, goethite α-FeOOH, lepidocrocite γ-FeOOH), Ca K-edge (calcite $CaCO_3$, oligoclase $(Ca,Na)(Si,Al)_4O_8$, anorthite $CaAl_2Si_2O_8$, gehlenite $Ca_2Al_2SiO_7$, wollastonite $CaSiO_3$, diopside $CaMgSi_2O_6$, merlinoite $K_5Ca_2Al_9Si_{23}O_{64} \cdot 24H_2O$), and K K-edge (kaliophilite $KAlSiO_4$, orthoclase $KAlSi_3O_8$, leucite $KAlSi_2O_6$, merlinoite), were prepared in the same manner to ensure consistency in measurement conditions. Standard spectra were collected in transmission mode at room temperature.

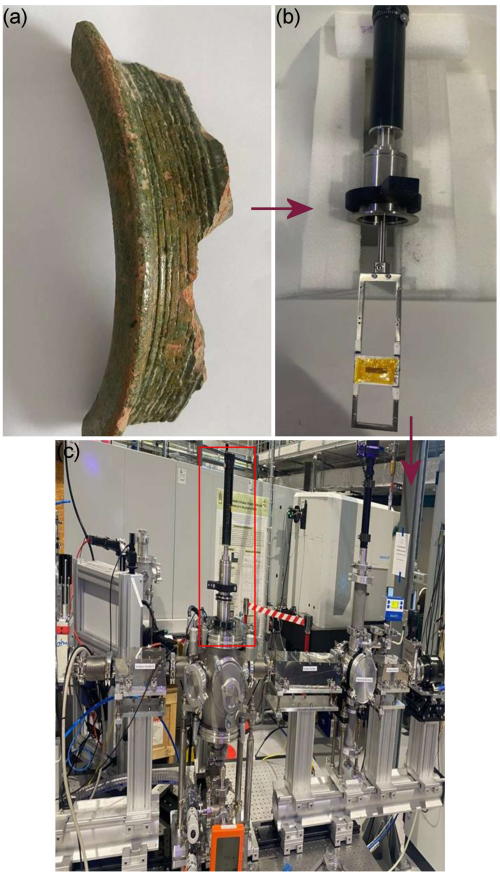

Fig. 7. Sample preparation and XANES analysis workflow. (a) A 16th-century pottery fragment, (b) powdered ceramic sealed between Kapton tape in a cylindrical holder for stable mounting, and (c) synchrotron XANES setup with the sample positioned in the beam path for fluorescence-mode K, Fe, and Ca K-edge measurements.

The number of reference phases used for linear combination analysis (LCA) was adjusted to the chemical complexity of each element system, reflecting the different oxidation states and coordination geometries present. Data processing and analysis were performed using the Athena program (version 0.9.26) from the Demeter software package for X-ray absorption spectroscopy (XAS) data analysis. The software is freely available and documented at [22] (see also [23]).

3. Multimodal result integration

To demonstrate the practical value of the sequential XRF → XRD → FTIR → Raman → XANES workflow, we present integrated results from a medieval ceramic fragment from the Żarska Cave and a piece of the 16th-century pottery from the Ojców Castle (southern Poland), analyzed through the first five methodological tiers.

3.1. XRF results (based on Sect. 2.3)

Representative XRF spectra (Fig. 8) confirm the compositional trends observed in the Żarska Cave ceramic, exhibiting a Si-dominated matrix (28.7 wt%) characteristic of a quartz-rich paste, along with consistent clay-derived impurities, including Al (7.9 wt%), Fe (6.1 wt%), K (4.2 wt%), Ca (2.1 wt%), and Ti (0.63 wt%). Key spectral features include Si K_α ($\sim$ 1.7 keV), Al K_α ($\sim$ 1.5 keV), Fe K_α (6.4 keV)/K_β (7.0 keV), Ca K_α ($\sim$ 3.7 keV), Ti K_α ($\sim$ 4.5 keV), together with trace Na K_α ($\sim$ 1.0 keV) and minor Pb L_α (10.6 keV). These spectral features indicate the alkali-rich bulk chemistry associated with the feldspar neoformation observed in subsequent XRD analysis, while guiding targeted phase identification.

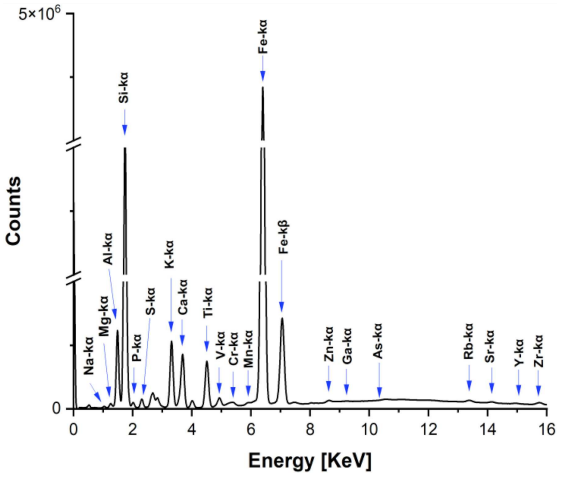

Fig. 8. XRF spectra of ceramic sample from the Żarska Cave.

3.2. XRD results (based on Sect. 2.4)

The XRD patterns (Fig. 9) recorded for the Żarska Cave ceramic fragment, from both surface and interior body, are dominated by a very intense diffraction peak at $2\theta \simeq 26.6°$ attributable to the (101) plane of α-quartz (SiO_2). This peak is identical in position, shape, and relative intensity across both profiles, confirming uniform quartz content and primary silicate framework throughout the sample, in full agreement with the silicate network features identified by FTIR. Accessory silicate phases differ subtly. The surface exhibits diffraction peaks attributed to $NaAl_3Si_3O_{11}$ (albite) and $FeSiO_3$ (ferrosilite), while the body is characterized by $K(Al,Fe)Si_2O_8$ (Fe-bearing orthoclase) and $(Na,Ca)Al(Si,Al)_3O_8$ (plagioclase) (e.g., intensity maxima within $2\theta \simeq 27°$–$28°$). These minor, location-specific phases suggest localized surface Na/Fe enrichment (possibly from cave fluids), but the core mineralogical composition including the dominant SiO_2 component remains homogeneous, with no evidence of secondary weathering products (e.g., gypsum or calcite overgrowths). The ceramic is thus well-preserved.

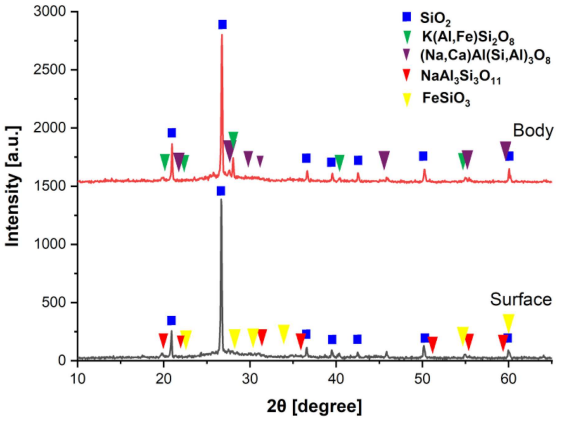

Fig. 9. XRD spectra of surface and body sites of ceramic sample from the Żarska Cave.

3.3. FTIR results (based on Sect. 2.5)

The main bands visible observed in all spectra (Fig. 10) in the 450–600 cm^{-1} range are mainly assigned to bending and stretching vibrations of the Si–O–Si and Al–O–Si network in silicates and aluminosilicates [24, 25]. These bands are characteristic of ceramic materials, clays, and quartz. The band around $\sim$ 700 cm^{-1} in FTIR spectra most often comes from lattice vibrations of metal–oxygen (M–O) bonds. Another prominent feature is the broad and strong band around 800–1100 cm^{-1}, typical of Si–O stretching vibrations in SiO_4 tetrahedra and representing the silicate frameworks; this serves as the main "fingerprint" of silicate minerals [26, 27]. In some samples, a weaker band can be observed near 1600 cm^{-1}, usually corresponding to the bending vibrations of -OH groups in adsorbed water.

FTIR spectra recorded for the Żarska Cave ceramic sample, collected from both the surface and interior (body) of the fragment, show no detectable changes in the position of bands characteristic of ceramic materials. This indicates that the mineralogical composition and structural features of the ceramic matrix remain consistent throughout the sample. The absence of additional absorption bands related to secondary mineral phases or alteration products suggests that no significant chemical transformation, weathering, or interaction with the cave environment has occurred. Therefore, the ceramic material appears to be well-preserved, with its original structural and compositional characteristics largely maintained.

3.4. Raman results (based on Sect. 2.6)

In the Raman spectra of the studied ceramic samples visible in Fig. 11, the low-frequency region around 110–160 cm^{-1} corresponds to lattice vibrational modes typical of oxide ceramics. These modes are characteristic of metal–oxygen M–O frameworks, such as those in TiO_2 (both anatase and rutile) and ZrO_2 (tetragonal or monoclinic) [28]. They represent external lattice vibrations and are often associated with translational movements of cations within the crystal structure. The group of bands observed between 440 and 465 cm^{-1} is one of the most distinctive features of oxide ceramics. The peaks in this region arise from strong M–O stretching vibrations within ordered lattices. They can correspond to the A_{1g} mode of Al_2O_3 near 451 cm^{-1} [29], the F_{2g} symmetric stretching mode of CeO_2 around 465 cm^{-1} [30], or the Si–O–Si bending vibration of SiO_2 at a similar position. In zirconia, comparable modes also occur in this range, making it a diagnostic region for identifying oxide phases [31]. Its presence strongly indicates that anatase titanium dioxide contributes to the Raman spectrum. The spectral region between 575 and 640 cm^{-1} reflects overlapping vibrational modes of several oxides. The band around 578 cm^{-1} is consistent with Al_2O_3 [25], while the features between 560 and 640 cm^{-1} correspond to ZrO_2 lattice modes [28]. The shoulder near 639 cm^{-1} again matches the characteristic E_g mode of anatase TiO_2, suggesting the coexistence of multiple oxide phases.

Raman spectra collected from both the surface and interior (body) of the ceramic fragment show very similar band positions in the analyzed spectral regions, indicating that the same oxide phases are present in both locations. The characteristic bands

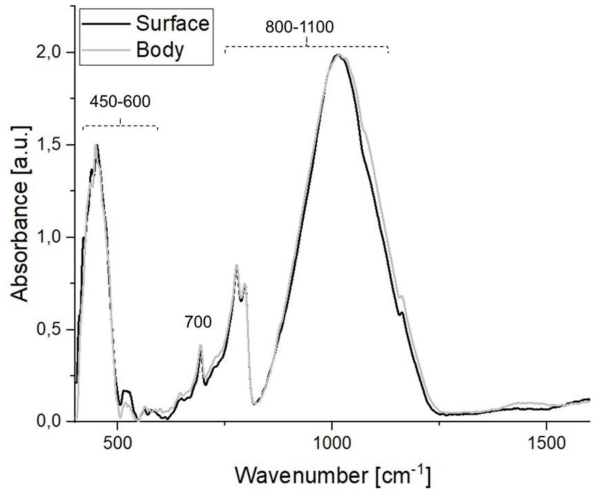

Fig. 10. FTIR spectra of the surface and body sites of a ceramic sample from the Żarska Cave.

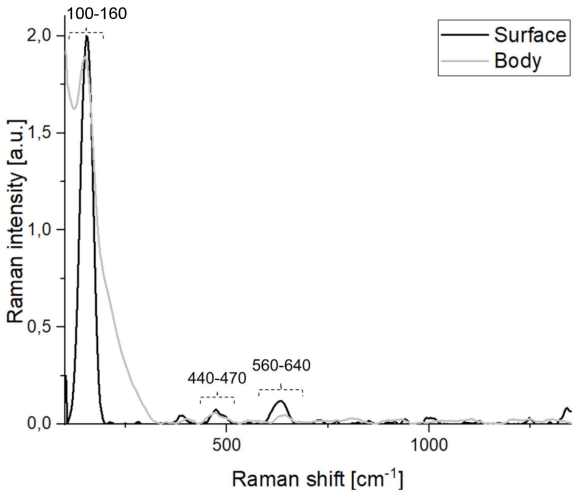

Fig. 11. Raman spectra of the surface and body sites of a ceramic sample from the Żarska Cave.

in the low-frequency region ($\sim$ 110–160 cm^{-1}), as well as those observed in the ranges 440–470 cm^{-1} and 560–640 cm^{-1}, appear in both spectra, confirming that the mineralogical composition and crystal structure remain consistent between the surface and the bulk material. The main differences are related to the relative intensities, and in the case of the range 560–640 cm^{-1}, the band positions. The surface spectrum exhibits slightly higher intensity in the regions around 440–470 cm^{-1} and 560–640 cm^{-1} compared to the body, which may suggest minor variations in the concentration or crystallinity of specific oxide phases (e.g., TiO_2 or ZrO_2) at the surface. However, these differences are subtle and do not indicate the presence of additional phases or secondary alteration products.

The absence of new Raman bands or significant spectral shifts between the surface and the body suggests that no substantial chemical transformation, weathering, or interaction with the surrounding environment has occurred. This confirms that the ceramic material is well-preserved, maintaining its original structural and compositional characteristics throughout the fragment.

3.5. XANES results (based on Sect. 2.9)

Ca K-edge XANES spectra (Fig. 12) of the Ojców (OJC_965) 16th century pottery reveal distinct calcium speciation between the body and the surface, completing the multimodal workflow. Linear combination fitting was applied using reference spectra of calcium sulfate ($CaSO_4$), calcium oxide (CaO), calcium carbonate ($CaCO_3$), and dicalcium silicate (Ca_2SiO_4) to quantify phase abundances in both regions.

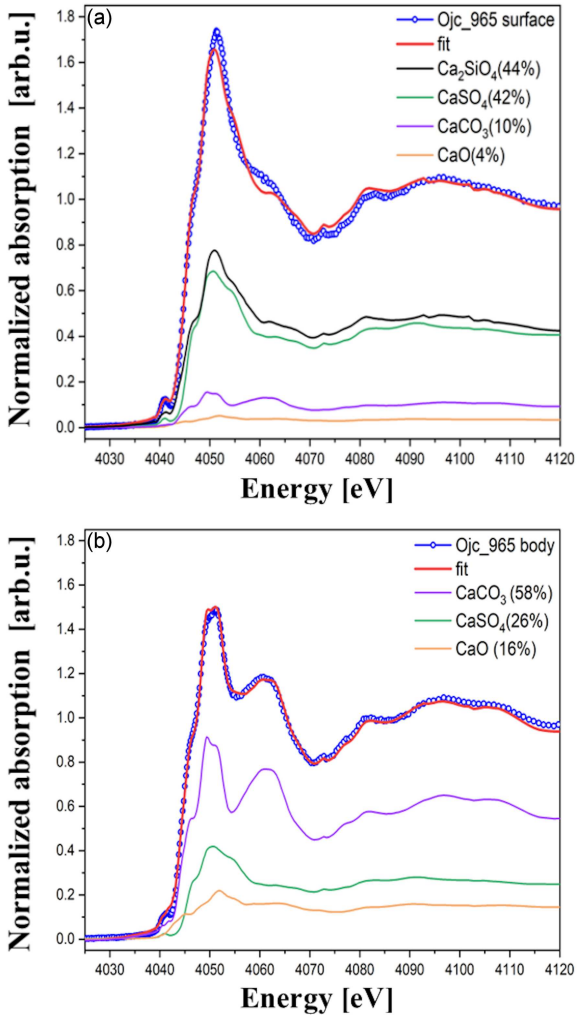

Fig. 12. XANES spectra of sites on the surface and body of the Ojców ceramic sample.

The surface is dominated by Ca_2SiO_4 (44%) and $CaSO_4$ (42%). This composition may indicate sulphate-rich fluxes, deliberately applied during glazing/processing, along with the significant neoformation of Ca_2SiO_4 from high-temperature lime–silica reactions characteristic of fritting processes ($\sim$ 900°C). Severely depleted $CaCO_3$ (10%) and CaO (4%) confirm substantial thermal decomposition of carbonates and lime consumption compared to the ceramic body. Conversely, the ceramic body preserves a stronger calcareous signature, dominated by $CaCO_3$ (58%) with moderate levels of $CaSO_4$ (26%) and CaO (16%). This composition reflects an original lime-rich marl composition fired at moderate temperatures ($\sim$ 800°C), retaining carbonate relics while forming minor sulphates from clay impurities or atmospheric reactions. The authors acknowledge that the available reference standards are limited and that future work will focus on acquiring additional reference measurements to expand the XANES reference library.

4. Conclusions

This study establishes a comprehensive sequential multimodal workflow for the archaeometric analysis of medieval ceramics, combining XRF, XRD, FTIR, Raman, SEM–EDS, XCT, and XANES to characterize elemental, crystalline, amorphous, microstructural, and chemical-state properties while preserving artefact integrity. XRF establishes baseline major (Si, Al, Fe, Ca, K, Na) and trace (Cr, Mn, Zr) profiles for paste discrimination, followed by:

- XRD identifying kaliophilite and oligoclase phases (consistent with firing temperatures $\sim$ 800–900°C),
- FTIR resolving amorphous networks (Si–O–Si, 950–1100 cm^{-1}),
- Raman detecting microscale oxide impurities, including TiO_2 (110–160 cm^{-1}), ZrO_2, Al_2O_3 (440–465 cm^{-1}), revealing heavy mineral tempers and refractory phases,
- SEM–EDS quantifying temper distributions,
- XCT revealing 3D void networks, and
- XANES speciating Fe^{2+}/Fe^{3+}, Ca carbonate–silicates, and K-feldspars.

This standardized framework enables precise reconstruction of provenance, fluxing strategies, pyrotechnology, and post-firing alterations beyond single and dual-technique limitations, providing a reproducible protocol for heritage science.

Acknowledgments

The subsidy of the Ministry of Science and Higher Education, grant no. 16.16.220.842, partially financed this study. This research project was supported/partly supported by the program "Excellence initiative — research university" for the University of Science and Technology. Raman spectroscopy and XANES measurements at the ASTRA beamline at the NSRC SOLARIS were made under the provision of the Polish Ministry and Higher Education project "Support for research and development with the use of research infra-structure of the National Synchrotron Radiation Centre SOLARIS", under contract no. 1/SOL/2021/2. The further development of the ASTRA beamline at the NSRC SOLARIS was supported within the EU Horizon 2020 program (952148-Sylinda).

References

[1] S. Scarcella, *Archaeological Ceramics: A Review of Current Research*, BAR Publishing, 2011.

[2] S. Dhanapandian, C. Manoharan, P. Sutharsan, *Acta Phys. Pol. A* **121**, 592 (2012).

[3] P. Colomban, A. Slodczyk, *Acta Phys. Pol. A* **116**, 7 (2009).

[4] P. Colomban, G. Simsek Franci, M. Gerken, M. Gironda, V. Mesqui, *Ceramics* **6**, 2178 (2023).

[5] C. Germinario, G. Cultrone, A. De Bonis, F. Izzo, A. Langella, M. Mercurio, L. Nodari, C.R. Vyhnal, C. Grifa, *Appl. Clay Sci.* **253**, 107347 (2024).

[6] A. Gianoncelli, S. Schöder, J.R. Plaisier, M. Fugazzotto, G. Barone, A. Russo, P. Mazzoleni, S. Raneri, *Heritage* **7**, 2118 (2024).

[7] C.L. Reedy, *Appl. Sci.* **12**, 11448 (2022).

[8] R. Abdelrahman, S. Wroński, M. Wojenka, J. Tarasiuk, L. Samek, *Nukleonika* **70**, 97 (2025).

[9] N. Henderson, T. Hill, D. Sampson, J. Sedlmair, *Am. Ceram. Soc. Bull.* **103**, 16 (2024).

[10] M.S. Rahman, H.S.C. Metselaar, B.B.A. Razak, *Mediterr. Archaeol. Archaeom.* **24**, 38 (2024).

[11] V. Papakosta, O. Lopez-Costas, S. Isaksson, *Archaeometry* **62**, 677 (2020).

[12] D. Bersani, P.P. Lottici, *J. Raman Spectrosc.* **47**, 499 (2016).

[13] C. Riera-Soto, C. Agüero, O. González-Maurel, M. Uribe, A. Menzies, *Front. Earth Sci.* **10**, 807865 (2022).

[14] Z. Li, X. Hu, X. Jiang, J. Cui, *Herit. Sci.* **12**, 1399 (2024).

[15] GE Sensing & Inspection Technologies phoenix X-ray GmbH, GE Computed Tomography, 2015.

[16] L.A. Feldkamp, L.C. Davis, J.W. Kress, *J. Opt. Soc. Am. A* **1**, 612 (1984).

[17] Volume Graphics GmbH, VGStudio Max Reference Manual Release 2.0, 2013.

[18] J. Szlachetko, J. Szade, E. Beyer et al., *Eur. Phys. J. Plus* **138**, 10 (2023).

[19] J. Hormes, W. Klysubun, J. Göttert et al., *Nucl. Instrum. Methods Phys. Res. B* **489**, 76 (2021).

[20] G. Cibin, A. Mottana, A. Marcelli, M.F. Brigatti, *Miner. Petrol.* **85**, 67 (2005).

[21] J. Rajendran, S. Gialanella, P.B. Aswath, *Mater. Sci. Eng. C* **33**, 3968 (2013).

[22] B. Ravel, Demeter software.

[23] B. Ravel, M. Newville, *J. Synchrotron Rad.* **12**, 537 (2005).

[24] F. Berna, A. Behar, R. Shahack-Gross et al., *J. Archaeol. Sci.* **34**, 358 (2007).

[25] S. Shoval, *J. Therm. Anal. Calorim.* **42**, 175 (1994).

[26] S. Shoval, *Opt. Mater.* **24**, 117 (2003).

[27] R. Ravisankar, A. Naseerutheen, G. Raja Annamalai A. Chandrasekaran, A. Rajalakshmi, K.V. Kanagasabapathy, M.V.R. Prasad, K.K. Satpathy, *Spectrochim. Acta A* **121**, 457 (2014).

[28] G. Pezzotti, A.A. Porporati, *J. Biomed. Opt.* **9**, 372 (2004).

[29] K. Delbé, C. De Sousa, F. Grizet, M. Yahiaoui, *Materials* **15**, 8645 (2022).

[30] V.V. Pushkarev, V.I. Kovalchuk, J.L. D'Itri, *J. Phys. Chem. B* **108**, 5341 (2004).

[31] P. Colomban, *Appl. Phys. A* **79**, 167 (2004).